Supplementary Material

1 FROM CORRELATION TO COHERENCE

1.1 Auto- and cross-correlation and power spectral density

The power spectral density of a real stationary signal $x(t)$ is defined as the Fourier transform of its auto-correlation $R_{xx}(t+\tau, t) = \mathbb{E}\left[x(t+\tau)x(t)\right]$:

$$S_x(f) = \int_{-\infty}^{\infty} R_{xx}(t+\tau, t) e^{-i2\pi f \tau} \mathrm{d}\tau, \tag{S1}$$

where $\mathbb{E}[z]$ describes the expected (mean) value of a random variable z (the signal is here treated as a stochastic process). Note that from the stationarity of the signal, $R_{xx}(t+\tau, t) = R_{xx}(\tau, 0)$ is independent of t and can be simply written $R_{xx}(\tau)$. In practice, $S_x(f)$ is often estimated by adapting the following expression:

$$S_x(f) = \lim_{T\to\infty} \frac{1}{T}\, \mathbb{E}\left[|\hat{x}_T(f)|^2\right], \tag{S2}$$

where $\hat{x}_T(f)$ is the Fourier transform of $x(t)$ restricted to the interval $[-\frac{T}{2}, +\frac{T}{2}]$: $\hat{x}_T(f) = \int_{-\frac{T}{2}}^{\frac{T}{2}} x(t) e^{-i2\pi f t}\mathrm{d}t$. Experimentally, the interval T remains finite and the ensemble average is replaced by the sample mean of a finite number of realizations, often subdivisions of a single longer stationary signal. The spectral density of a real signal is real, non-negative and symmetric: $S_x(f) \in \mathbb{R}$, $S_x(f) \geq 0$, $S_x(-f) = S_x(f)\ \forall f \in \mathbb{R}$.

Finally, if we assume that the stationary signal $x(t)$ is ergodic, ensemble averages $\mathbb{E}[x]$ are equivalent to temporal averages $\langle x \rangle_T = \lim_{T\to\infty} \frac{1}{T} \int_{-\frac{T}{2}}^{\frac{T}{2}} x(t)\mathrm{d}t$ and the auto-correlation and $R_{xx}(\tau) = \mathbb{E}[x(\tau)x(0)] = \langle x(t+\tau)x(t)\rangle_T$. The case $\tau = 0$ relates the power spectral density to the power of the signal $\langle x(t)^2\rangle_T = \int_{-\infty}^{\infty} S_x(f)\mathrm{d}f$; it is a form of Parseval's identity. When the signal is of zero mean, $\mu_x = \mathbb{E}\left[x(0)\right] = 0$, its variance $\sigma_x^2 = R_{xx}(0) - \mu_x^2$ identifies to its power.

The cross power spectral density of two real stationary signals $x(t)$ and $y(t)$ is defined similarly from their cross-correlation $R_{xy}(t+\tau, t) = \mathbb{E}\left[x(t+\tau)y(t)\right]$:

$$S_{xy}(f) = \int_{-\infty}^{\infty} R_{xy}(t+\tau, t) e^{-i2\pi f \tau} \mathrm{d}\tau. \tag{S3}$$

It takes complex values, has the Hermitian symmetry, $S_{xy}(-f) = \overline{S_{xy}}(f)$ (the bar denotes the complex conjugation), and it can also be written from the Fourier transforms of $x(t)$ and $y(t)$: $S_{xy}(f) = \lim_{T\to\infty} \frac{1}{T}\, \mathbb{E}\left[\hat{x}_T(f)\overline{\hat{y}_T}(f)\right]$.

1.2 Covariance, correlation coefficient and complex version

From the cross-covariance of two real signals $x(t)$ and $y(t)$: $c_{xy}(t+\tau,t) = \mathbb{E}\left[(x(t+\tau) - \mu_x(t+\tau))\right.$ $\left.(y(t) - \mu_y(t))\right] = R_{xy}(t+\tau,t) - \mu_x(t+\tau)\mu_y(t)$, one can define their correlation coefficient (Pearson):

$$\rho_{xy}(t+\tau,t) = \frac{c_{xy}(t+\tau,t)}{\sigma_x(t+\tau)\sigma_y(t)}, \tag{S4}$$

which quantifies the strength of the linear relationship between x and y, and takes values in the interval $[-1,1]$. A value of 1 (respectively -1) indicates a full linear correlation (resp. anti-correlation), while a zero value indicates the absence of linear correlation. Although this expression is valid for non-stationary signals, their stationarity is often assumed, at least locally, to estimate the averages in a single trial experiment. In this context, the correlation coefficient and the cross-covariance are quantities which focus on the similitude of the signals in time and its variation with respect to τ, sign of synchronization or delay between similar components. It is however difficult to discriminate the influence of the signals spectral signature (which also depends on the recording methods for physiological rhythms) or the contributions of independent components of distinct frequencies.

If the two stationary signals x and y are of zero mean, the correlation coefficient $\rho_{xy}(\tau) = \rho_{xy}(\tau,0)$ identifies to the cross-correlation normalized by the auto-correlations. We can use their Fourier relation (inverse transform) to the spectral densities to rewrite the correlation coefficient:

$$\rho_{xy}(\tau) = \frac{R_{xy}(\tau)}{\sqrt{R_{xx}(\tau)R_{yy}(\tau)}} = \frac{\int_{-\infty}^{\infty} S_{xy}(f)e^{i2\pi f\tau}\mathrm{d}f}{\sqrt{\int_{-\infty}^{\infty} S_x(f)\mathrm{d}f \int_{-\infty}^{\infty} S_y(f)\mathrm{d}f}}. \tag{S5}$$

In this expression, a mixture of frequency components participates to the resulting correlation coefficient.

Exploiting the symmetry of positive and negative frequency components of the spectral densities of real stationary signals, we can rewrite the correlation coefficient as the real part $\rho_{xy} = \Re\{\rho^*_{xy}\}$ of the following complex quantity:

$$\rho^*_{xy}(\tau) = \frac{\int_0^{\infty} S_{xy}(f)e^{i2\pi f\tau}\mathrm{d}f}{\sqrt{\int_0^{\infty} S_x(f)\mathrm{d}f \int_0^{\infty} S_y(f)\mathrm{d}f}}. \tag{S6}$$

This is a complex extension of the correlation coefficient that takes values in the unit disk: $\rho^*_{xy} \in \mathbb{C},\ |\rho^*_{xy}| \leq 1$. Equivalently, ρ^*_{xy} is the correlation coefficient between the analytic versions of the signals $x,\ y$ (extended to complex helical signals by removing their negative frequency components). The additional information contained in its imaginary part is useful to characterize phase quadrature phenomena such as the one between a deterministic component and its derivative: $x(t) = \frac{\mathrm{d}}{\mathrm{d}t}y(t) \ \Rightarrow\ S_{xy}(f) = i2\pi f S_y(f) \ \Rightarrow$ $\rho^*_{xy}(0) = i = e^{i\frac{\pi}{2}}$. This extends the idea of full correlation to the condition $|\rho^*_{xy}| = 1$, letting the phase indicates if this is a positive correlation, an anti-correlation (phase opposition $\pm\pi$) or a phase quadrature ($\pm\frac{\pi}{2}$) as in this example.

The properties of this complex correlation will extend to the spectral coherence, so that ρ^*_{xy}, as a precursor, can be called the global coherence of the pair of stationary real signals x and y.

1.3 Spectral and time-frequency coherence

The coherence measure between two signals at frequency f is a further extension of the Pearson correlation coefficient and was initially defined as the absolute square of their cross-spectrum divided by their auto-spectra. Consider two jointly stationary, zero-mean, real random processes with signals $x(t)$ and $y(t)$, their spectral coherence (sometimes called coherency function) (Gardner, 1992):

$$\gamma_{xy}(f) = \frac{S_{xy}(f)}{\sqrt{S_x(f)S_y(f)}}, \tag{S7}$$

is the cross spectral density of $x(t)$ and $y(t)$ normalized at each frequency component. It takes complex values in the unit disk, and the squared coherence, $|\gamma_{xy}(f)|^2 \leq 1$, represents the proportion of the power of one signal at frequency f that can be linearly predicted from the other signal. Notice the similarity with the interpretation of the correlation coefficient.

Although it does not appear as a variable here, the presence of a delay, can be recovered from the phase $\phi(f)$ of the spectral coherence: $\gamma_{xy}(f) = |\gamma_{xy}(f)|e^{i\phi(f)}$. Indeed, consider that the signals are shifted copy of each other, $x(t) = y(t+\tau)$, then their coherence is simply $\gamma_{xy}(f) = e^{i2\pi f\tau}$: x is early of τ as compared to y (*i.e.* y is late of τ). Thus, a spectral phase relation between the signals of the form $\phi(f) = \phi_0 + 2\pi f\tau$ is interpreted straightforwardly, as a delay τ between them as in the above example, and as phase shift ϕ_0 as for the phase of the complex correlation coefficient ρ^*_{xy}. The interpretation is as exact as the coherence modulus $|\gamma_{xy}(f)|$ is close to 1. See reference (Carter, 1987) for an extended statistical analysis.

The time-frequency coherence quantifies the strength of correlation between non-stationary signals and can be defined as:

$$\gamma_{xy}(f,t) = \frac{S_{xy}(f,t)}{\sqrt{S_x(f,t)S_y(f,t)}}, \tag{S8}$$

where $S_{xy}(f,t),\ S_x(f,t)$ and $S_y(f,t)$ stand for the non-stationary cross- and auto-spectra of the two signals x and y. Their definition relies both on a time-frequency distribution and on an averaging or filtering method to get estimators in the case of single trial experiments. Several methods have been proposed based on smoothed Wigner-Ville distributions, multi-taper spectrograms (Walden, 2000) and smoothed or multiple wavelet transforms (Orini et al., 2012; Keissar et al., 2009).

2 STATISTICAL ESTIMATION OF THE SIGNIFICANCE FOR THE TIME-FREQUENCY COHERENCE

The study of the statistical distribution for the estimator (Eq. (18)) of the time-frequency coherence $\gamma_{xy}(f,t)$ is essential to assess the significance of the result. The properties of the noisy background in each signal of interest directly influences this distribution. The coherence of a pair of background noises is called the spurious coherence γ_{sp}, its phase is uniformly distributed. The distribution of its squared modulus $|\gamma_{\text{sp}}|^2$ is used to build the significance level of a squared coherence $|\gamma_{xy}(f,t;\psi,\chi)|^2$ estimated between two signals with such background noises. Furthermore, the spurious coherence level is also greatly affected by the choice of the wavelet ψ_Q and time-smoothing kernel χ_n: the higher the number of wavelets that fits in the smoothing kernel (described by the parameter n), the more significant the estimated coherence, but also the lower its time resolution.

A theoretical framework is luckily available in reference (Cohen and Walden, 2010a,b) for the distribution of the estimator, both for the multi-wavelet and the time-smoothing methods, under the assumptions of jointly stationary and Gaussian noises. These assumptions are appropriate to describe the ambient or instrumental noise present in the physiological recordings. Their general result is as follows: the squared spurious time-frequency coherence estimator is distributed according to a so-called Goodman distribution, that depends on two parameters. The first one is the (exact) spectral coherence $|\gamma_{\text{sp}}(f)|^2$ of the pair of jointly stationary noises, and the second parameter is a number of degree of freedom that depends on the frequency, the wavelet and the smoothing kernel.

For the sake of simplicity, we further assume the independence of the noises, *i.e.* $|\gamma_{\text{sp}}(f)|^2 = 0$. The Goodman distribution then reduces to a particular beta distribution $\mathcal{B}(1, \beta)$ for the squared spurious coherence remaining in the time-frequency estimator, of mean and cumulative distribution (Gish and Cochran, 1988):

$$\mathbb{E}[|\gamma_{\text{sp}}|^2] = \frac{1}{\beta + 1} \tag{S9}$$

$$\Pr(|\gamma_{\text{sp}}|^2 \leq \gamma^2) = 1 - (1 - \gamma^2)^{\beta} \quad , \tag{S10}$$

where $\beta + 1$ can be interpreted as a degree of freedom (Cohen and Walden, 2010a,b). Note that the assumptions of independent, jointly stationary and Gaussian noises can be difficult to test and even incorrect in many cases. In the absence of more information, this remains an effective method that we can interpret as giving the minimum expected level of spurious coherence. This approach is considered as sufficient for the aim of our study, and can be checked by comparing coherence results with the coherence of surrogates.

Next, rather than looking for an analytical expression of $\beta = \beta(f, Q, n)$, which would not account for the effect of the discretization of continuous expressions in numerical computations, we prefer to estimate β from a simulation of the spurious coherence. Eq. (S9) provides a simple relation between β and the squared spurious coherence averaged over all times: $\beta(f, Q, n) + 1 = \langle|\gamma_{\text{sp}}(f, t; Q, n)|^2\rangle_T^{-1}$. In Fig. S1, we illustrate an estimation for two independent white Gaussian noise signals (real and normal) of length 2^{20}, with a time step such that their sampling is 500Hz.

An obvious property of our time-frequency coherence estimator is the absence of frequency dependence $\beta = \beta(Q, n)$, as can be observed in the density map of Fig. S1(B) obtained from histograms of $|\gamma_{\text{sp}}(f, t; Q, n)|^2$ for each frequency. This is due to our choice of time-smoothing definition (Eq. (15)), adapted to the wavelet in a scale-invariant way. Other forms of smoothing of the CWT, for instance at a constant time resolution, would necessarily yield a decreasing significance at low frequencies, as described in references (Torrence and Compo, 1998; Gurley et al., 2003).

Exploiting this property, the data aggregated from all frequencies can be merged to estimate $\beta(Q, n)$ from the time-frequency average $\langle|\gamma_{\text{sp}}(f, t; Q, n)|^2\rangle_{F,T}^{-1}$. A sufficient time resolution (more than 10 per wavelet resolution δt) and suitable frequency integration depending on the frequency sampling ($\iint \mathrm{d}f\mathrm{d}t = \iint f\mathrm{d}t\mathrm{d}\log f$) are critical aspects of this estimation. Its precision is strikingly illustrated in Fig. S1(D), where the sample cumulative distribution and the beta distribution with the estimated degree of freedom are precisely superimposed (as well as their quantile-quantile plot in the inset).

When varying Q and n, the degree of freedom is actually observed to be very close to n, which by construction is an effective duration of the Gaussian smoothing kernel χ_n in unit of wavelet width (the

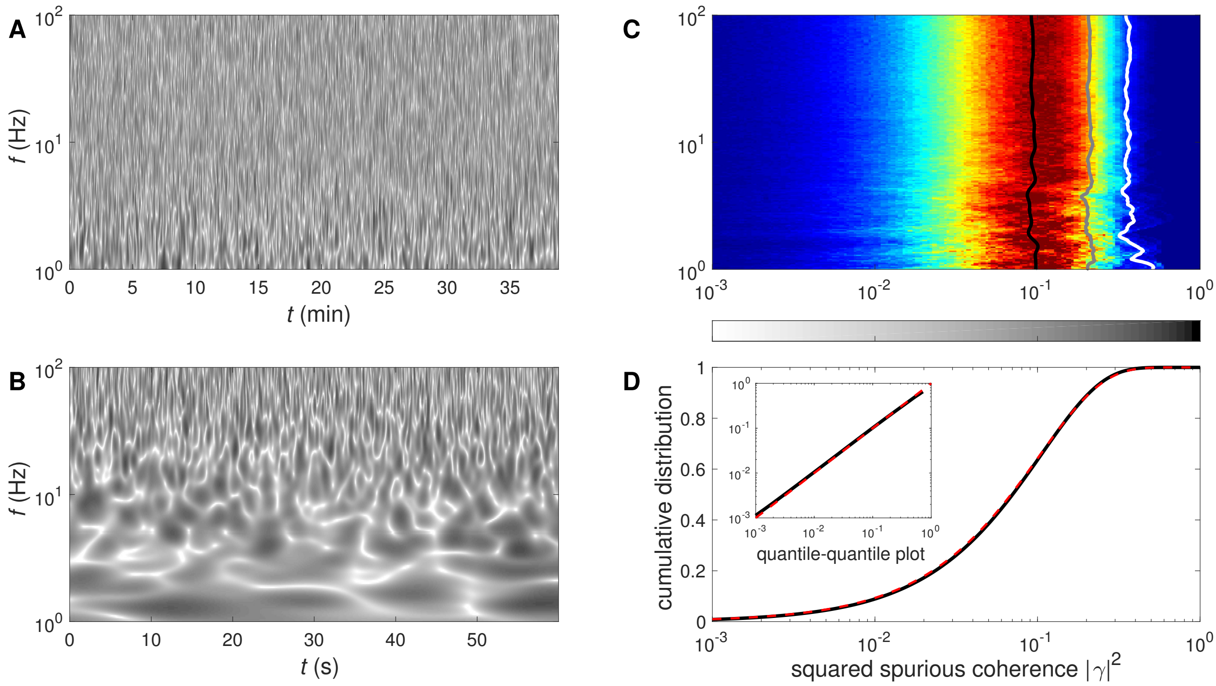

Figure S1. Estimation of the squared spurious coherence distribution simulated from two independent white Gaussian noises. The CWT of the noises are computed with a Grossmann wavelet of quality factor $Q = 5$, and their spectral densities are estimated from the Gaussian time-smoothing kernel χ_n of parameter $n = 10$. (A) Image of the squared spurious coherence of a single simulation in time and frequency. (B) Zoom on a shorter time scale, showing the characteristics of the time-smoothing (Eq. (15)). The colour bar associated to the value of the squared coherence in (A) and (B) is aligned with the x-axes of (C) and (D). (C) Density map that represents the distribution of the squared spurious coherence collected at all times for each fixed frequency. A horizontal slice of this density map at a certain frequency thus corresponds to a histogram: red indicates a high density and blue a low density. The black line indicates its mean for each frequency, the grey line is the quantile at 0.9 and the white line is the quantile at 0.99. (D) Sample cumulative distribution of the simulated squared spurious coherence (black line), adjusted with a beta distribution $\mathcal{B}(1, \beta)$ of estimated parameter $\beta = 9.8$ (red dashed line), see definition (S10). The inset represents the quantile-quantile plot of the sample versus beta estimated distributions (black line). The alignment with the ideal case (red dashed line) indicates a very good agreement.

quality factor appears in the time-smoothing kernel definition Eq. (17) for this reason). On one hand, we observe a weak dependence on the quality factor, $\beta(Q, n) \approx \beta(n)$: for instance $\beta(Q = 5, n = 10) = 9.8 \pm 0.1$ and $\beta(Q = 10, n = 10) = 9.7 \pm 0.1$ in our numerical implementation. On the other hand, high n values (such as $n = 20,\ 50, ...$) are practically indistinguishable from the estimated parameter: $\beta \approx n$. For lower values of n, however, we clearly observe $\beta < n$.

Eventually, we assess and confirm the robustness of the spurious coherence insensitivity to the colour (*i.e.* the auto-covariance) of Gaussian independent noises, especially in the case of the pink noise used in Fig. 2 that has a particular relevance to the analysis of EEGs (with the same spectral trend). We notice that coherence estimators based on a time-frequency smoothing do not have this useful property.

Significance levels correspond to p-values and are easily derived from the beta distribution (S10):

$$p(\gamma^2) \equiv \Pr(|\gamma_{\text{sp}}|^2 > \gamma^2) = (1 - \gamma^2)^\beta \tag{S11}$$

$$\gamma^2(p) = 1 - p^{\frac{1}{\beta}}. \tag{S12}$$

Thus, the threshold for observing a significant time-frequency coherence between some signals $x(t),\ y(t)$ with smoothing parameter $n = 10$ and p-value $p = 0.1$ (90% level of significance): $|\gamma_{xy}(f,t)|^2 > 1 - 0.1^{\frac{1}{\beta}} \approx 0.2$. A coherence analysis with $n = 10$ would have a good time-resolution but would detect only significant coherence of modulus $|\gamma_{xy}(f,t)| \gtrsim 0.5$. In contrast, 5 times lower ($n = 50$) temporal resolution would distinguish a coherence of modulus near 0.2 as significant ($p < 0.1$), and a coherence of modulus 0.5 with an very high significance, $p(0.5^2) < 10^{-6}$.

The beta distribution was already proposed to evaluate the significance of the time-frequency coherence in the context of a multi-wavelet estimator (Brittain et al., 2007), as an extension of the spectral coherence significance. Its origin lies in the characterization of the significance for the sample estimator of the correlation coefficient; for two independent random Gaussian vector of length N, we have the spurious correlation $|\rho_{\text{sp}}|^2 \sim \mathcal{B}(\frac{1}{2}, \frac{N}{2} - 1)$, and its complex extension $|\rho^*_{\text{sp}}|^2 \sim \mathcal{B}(1, \frac{N}{2} - 2)$.

As a last remark, the homogeneity of the coherence significance in the time-frequency plane meets a practical limitation at numerical borders, such as initial and final times, and the Nyquist frequency (half of the sampling frequency f_S of the signals). When approaching these borders in the range of the coherence resolutions $n\delta t$ and $\delta \log f$, the significance significantly drops. This distance to time limits is materialized by lines (sometimes called the cones of influence) and the maximum frequency is reduced to $f_S/2e^{\delta \log f}$.

3 COMPLEX RATE COMPUTATION FOR A PULSED MODEL SIGNAL

To further test the complex rate $\mathcal{K}$ (Eq. (8)) in a situation of strong non-linearity, we define a second type of model signals, $x(t) = z(\phi(t))$ and $y(t) = A(t)z(2\pi f_0 t)$ where $A(t),\ \phi(t)$ are the amplitude and phase defined in Eqs. (10,11). The oscillation $z(t)$ is now a periodic rectangular pulse train, 10% of the cycle at value 1, 0 otherwise, which is much more non-linear than the triangle wave of Fig. 3. The main effect of this stronger non-linearity is the presence of a larger oscillation at the rhythm's frequency in both the real and part imaginary parts $\mathcal{K}_{\text{R}}(t),\ \mathcal{K}_{\text{I}}(t)$, as can be observed in Fig. S2 (black lines in all panels). The overestimation of the ideal frequency modulation $\dot{\phi}(t)/2\pi$ by $\mathcal{K}_{\text{I}}(t)/2\pi$ is also increased with the rectangular pulses as compared to the triangle wave. These effects are due to the high amplitude of the harmonic frequencies; thus, we attempt to attenuate them using a modified weight function in the frequency average Eq. (7). In particular, we apply an additional power law decay to the signal's CWT and hence to the frequency weight: $w(f) = |f^{-2}X_Q(f,t)|^2$. While the reduction of the fast oscillation and bias is effective on this model signal, the change of the weight function $w(f)$ perturbs the estimation of the amplitude modulation, that behaves in Fig. S2(A) as the opposite of the frequency modulation Fig. S2(B). In a practical application, we can also expect an amplification of noisy fluctuations slower than the fundamental frequency of the rhythm.

4 SUPPLEMENTARY CWTS OF MODEL AND POLYSOMNOGRAPHY SIGNALS

4.1 Simple model for a quasi-steady physiological state

The rhythms observed in some selected time intervals, such as in the NREM sleep stage 2, can exhibit few to no non-stationary features. This is illustrated in Figs S3 and S4. In such condition, the power spectral density of the signal (or its log-frequency version $S_x(f)f$ as in Fig. S4(B,D,F) captures most of the rhythmic information. While it offers a synthetic representation of the rhythmic frequency and amplitude/power, it lacks subtle features, such as the modulation at the respiratory frequency of the ECG amplitude, visible in Figs. S3(C) and S4(C) (but not in S4(D)). This slight rhythmic modulation constitutes

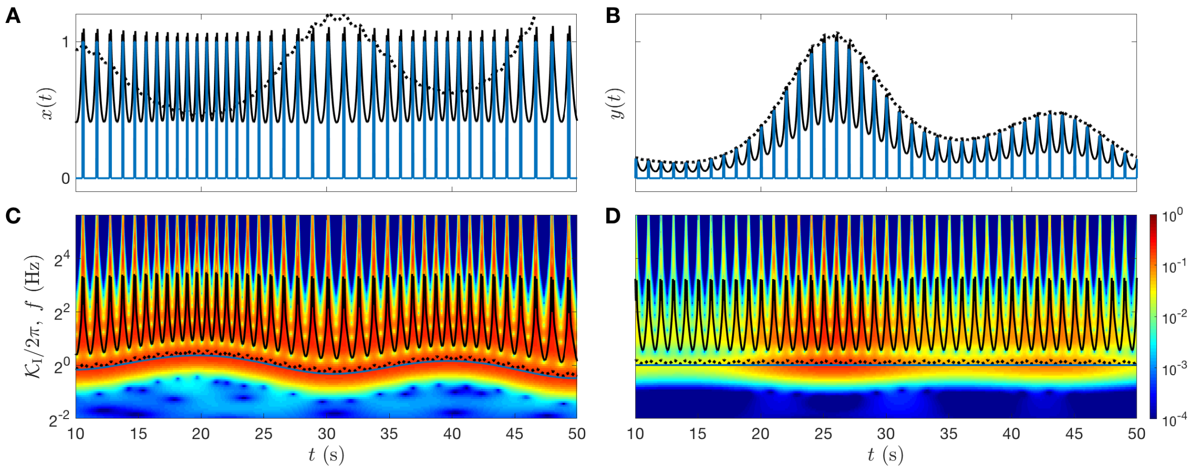

Figure S2. Comparison of two frequency weight functions for estimating the complex rate of an idealized modulated signal. Rectangular pulse trains, **(A)** of modulated frequency and constant amplitude, **(B)** of constant frequency and modulated amplitude (blue lines) with their amplitude modulation $\tilde{A}(t)$ (black lines) estimated from Eq. (12) using $\mathcal{K}_{\mathrm{R}}(t)$. The black dotted lines are alternative estimations (see details below). **(C,D)** Amplitude of the CWTs of the two signals, $2|X_Q(f,t)|$, with their frequency modulations estimated as the imaginary parts of the complex rates (Eq. (8)), $\mathcal{K}_{\mathrm{I}}(t)/2\pi$ (black lines), the ideal values (blue line), and the alternative estimations (black dotted line). In all panels, black lines are computed with the frequency weighting as in Eq. (8), whereas black dotted lines aim at reducing the non-linearity-induced oscillations and bias by using a high frequency attenuation with the frequency weight function: $w(f) = |f^{-2}X_Q(f,t)|^2$. The Grossmann wavelet of quality factor $Q = 5$ is used for the CWTs and for the rates computations.

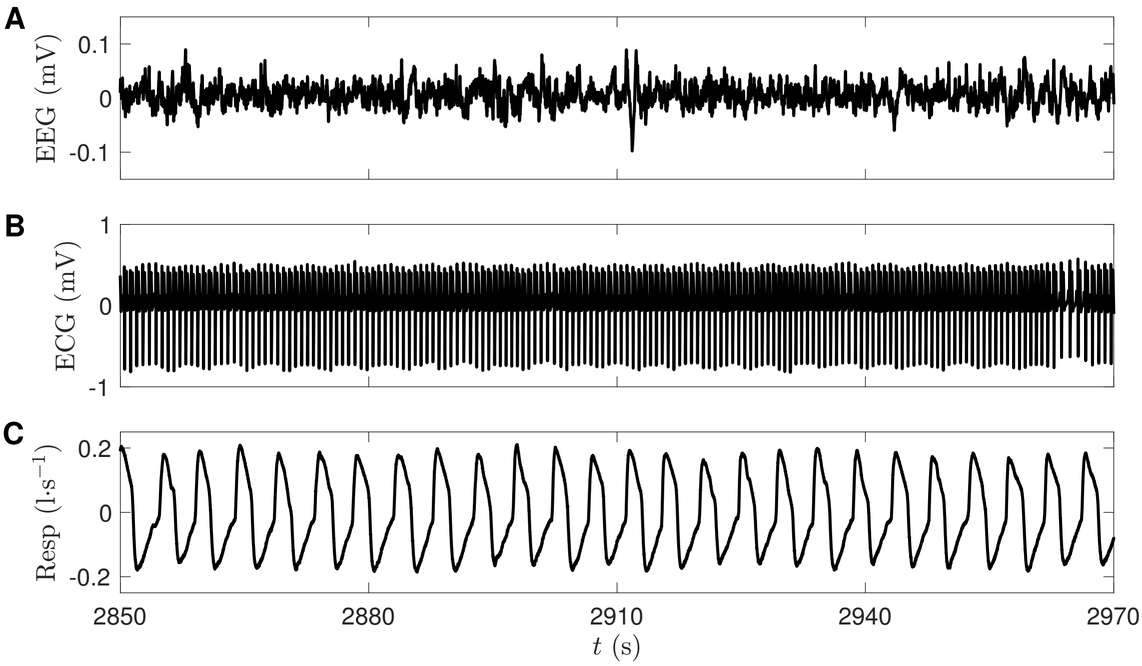

Figure S3. Zoom on a selected time interval of the three polysomnographic signals of subject *slp04* from the database *slpdb* during the NREM sleep stage 2. **(A)** EEG (C3-O1) in millivolt, **(B)** ECG in millivolt, and **(C)** nasal respiration in litre per second.

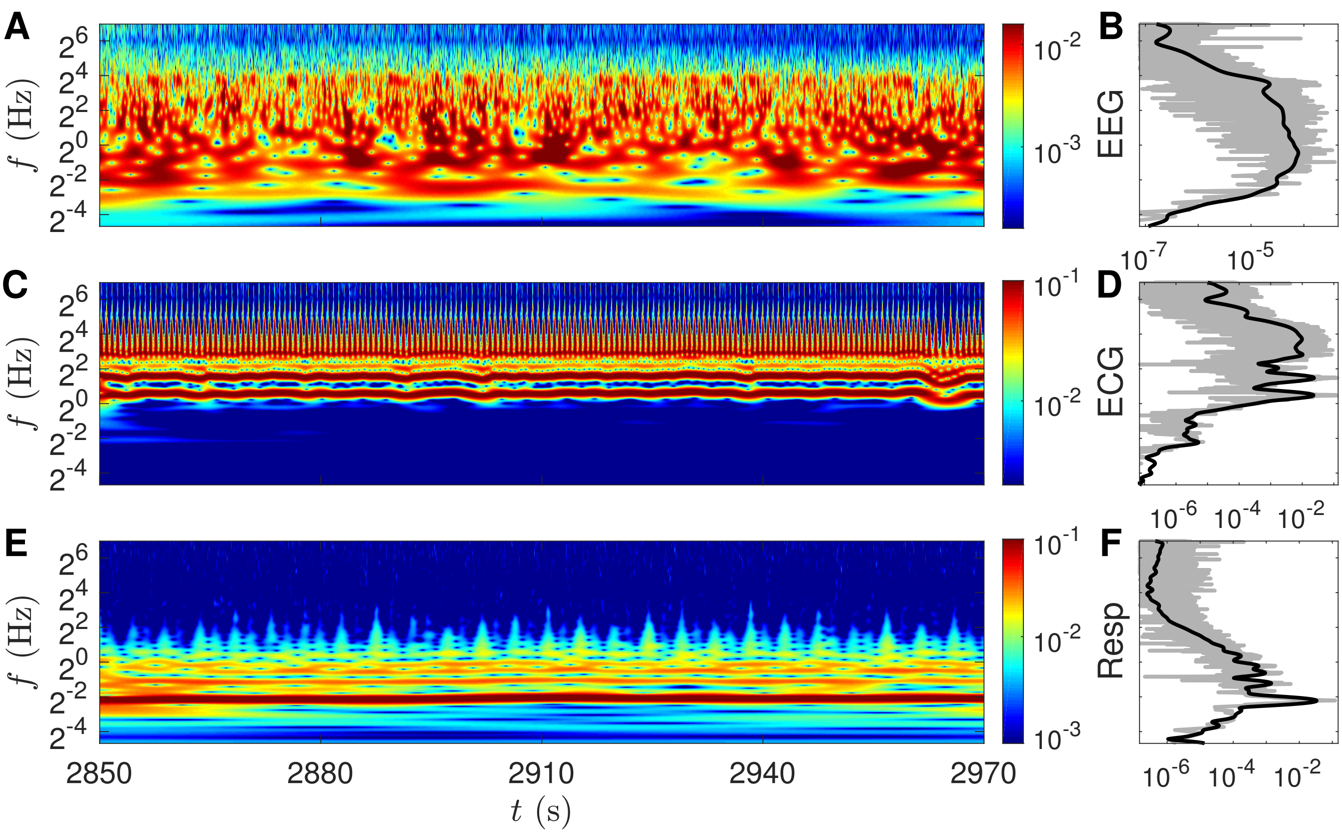

Figure S4. CWT **(B,D,F)** and spectral densities **(C,E,G)** of the physiological signals from Fig. S3. During this selected time interval, the person is in the NREM sleep stage 2. **(A)** CWT of the EEG (C3-O1) (amplitude in mV) and **(B)** power log-frequency density (in mV^2). **(C)** CWT of the ECG (amplitude in mV) and **(D)** power log-frequency density (in mV^2). **(E)** CWT of the nasal respiration signal (amplitude in l·s^{-1}) and **(F)** power log-frequency density (in (l·s^{-1})^2). Each CWT is computed with the Grossmann wavelet of quality factor $Q = 5$. The corresponding power log-frequency density $S_x(f)f$ is estimated either directly from the Fourier transform (thin gray line) or from the CWT as in Eq. (1) (thick black line).

an information which is accessible via time-frequency methods such as the complex rate computation introduced in Eqs (7-9).

Therefore, steady physiological rhythms are not stationary enough to be fully described by spectral methods.

4.2 CWTs of EEG, ECG and respiration recordings

Fig. S5 presents the CWTs of the overnight polysomnographic recordings that serve to compute the coherence of the raw signals (see Fig. 9). At this over-night time scale, the states of wake-sleep are easily observable in the CWT (Fig. S5(A), comparable with the hypnogram). Fig. S5(D) shows the effect of shuffling uniformly the phase of the EEG signal in the Fourier domain: the initial signal is “stationarized” while the global spectral density is conserved, yielding its phase-randomized surrogate.

Computing such a large CWT is extensive in memory, and managed by a careful time-frequency sampling that approximates the scale-free CWT resolution. The frequency domain is divided into frequency bands of an octave in which the wavelet transform is estimated as distinct matrices, with a geometric frequency sampling (accounting for the log-frequency resolution $\delta \log f = \frac{\sqrt{2\pi}}{Q}$ of $\hat{\psi}_Q$) and a linear time sampling

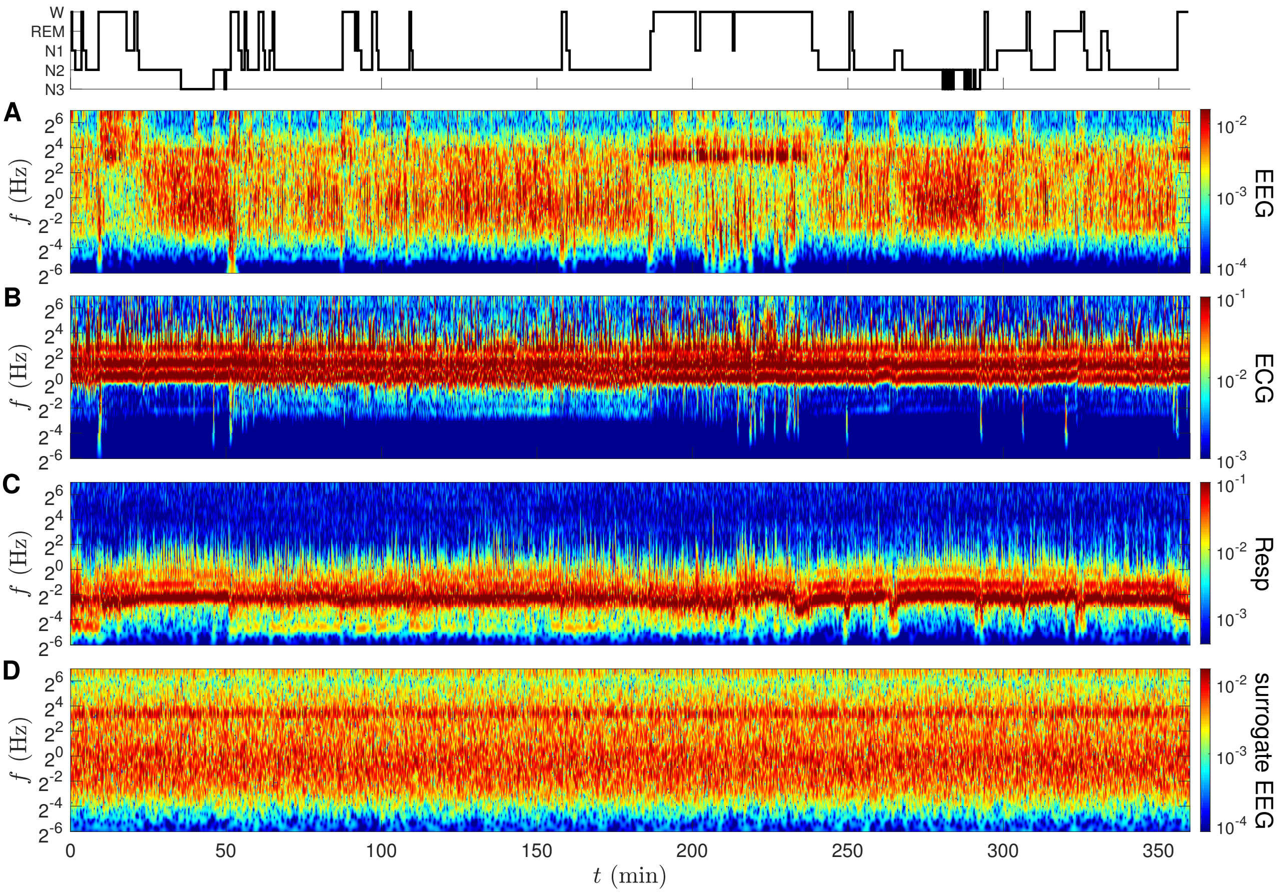

Figure S5. CWT of the overnight records for subject *slp04* from the database *slpdb*. **(A)** EEG (C3-O1), **(B)** ECG, **(C)** respiration signal, **(D)** surrogate signal of the EEG. The colour codes for the amplitude (twice the modulus) of the CWT, are computed with the Grossmann wavelet of quality factor $Q = 5$. The amplitudes have the dimension of the signal: all are in millivolt (mV), except for the respiration signal which is in litre per second ($\mathrm{l{\cdot}s^{-1}}$). The lowest amplitude in the colour bar corresponds to the resolution of the signals.

(both smaller than the wavelet resolution for smoothness). Starting from the highest octave: each time we compute the next matrix an octave below, we down-sample it in time by a factor 2 (akin to the discrete orthogonal wavelet transform). This accounts for the time resolution $\delta t = \frac{Q}{f\sqrt{2\pi}}$ of ψ_Q. In this way, no memory is wasted on unnecessary precision of time or frequency smoothness. Note that a sufficient time sampling is critical to the coherence estimation from the time-smoothing method.

5 INTER-BAND EEG COHERENCE

In complement to the time-frequency coherence of selected rate signals of Fig. 10, we provide here the CWT computed for the amplitude modulation in each band, Fig. S6, and the coherence of all the pairs of EEG band modulations, Fig. S7.

As expected, we do not observe band modulation frequencies higher than the upper frequency of the corresponding band. This is due to the smoothness property of the CWT.

The “apneic rhythm” around 0.035Hz between 50 and 180min (NREM sleep stage 2) can be noticed on the CWTs and is very coherent in all pairs, each with a typical phase shift. The wake state is characterized

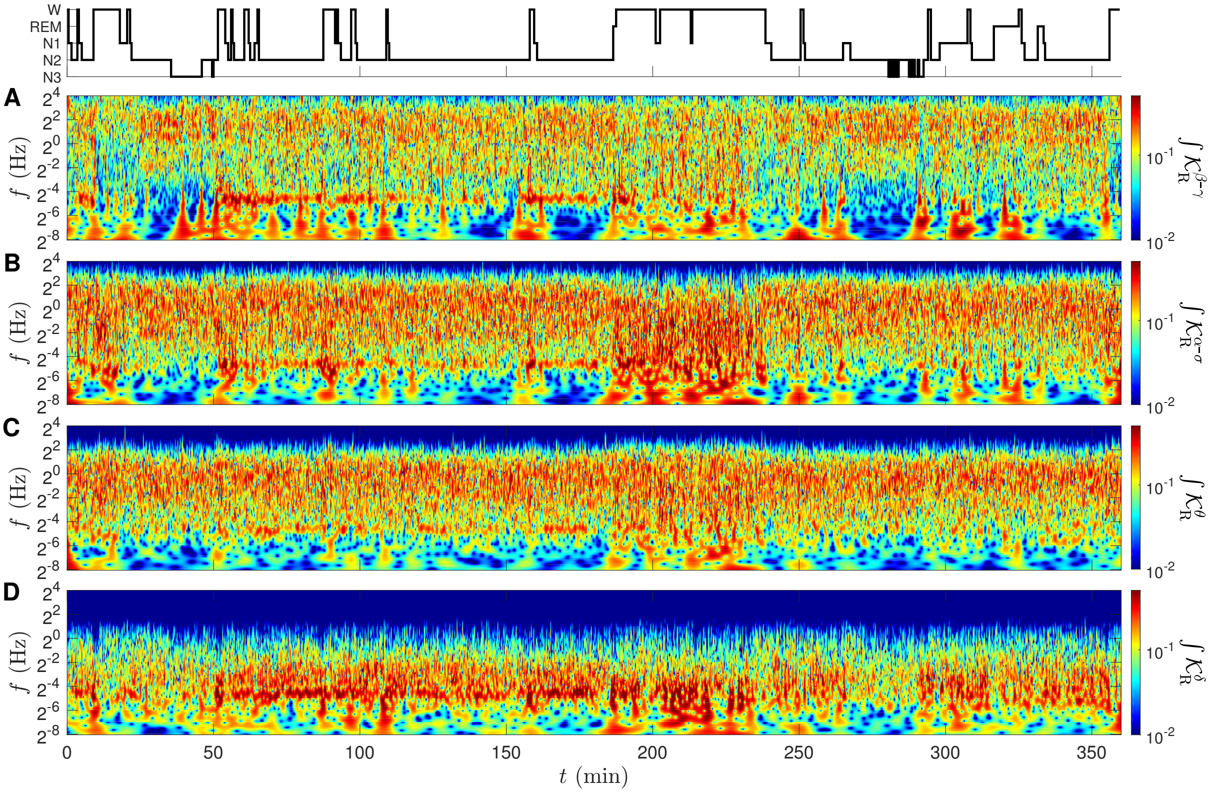

Figure S6. CWT of the amplitude modulations in different EEG bands for subject *slp04* from the database *slpdb*, estimated from the real part of the complex rate (Eqs. 8,9) as $\int \mathcal{K}_{\mathrm{R}}^{\mathrm{band}}$. Amplitude modulations of: **(A)** the $\beta - \gamma$ band (125 to 16Hz), **(B)** the $\sigma - \alpha$ band (16 to 8Hz), **(C)** the θ band (8 to 4Hz), **(E)** and the δ band (4 to 1/4 Hz). The colour codes for the amplitude (twice the modulus) of the CWT, computed with the Grossmann wavelet of quality factor $Q = 5$, which has no dimension here.

by more intense modulations in the $\alpha - \sigma$ band (Fig. S6(B)) and a strong in-phase coherence (green) between the θ and $\alpha - \sigma$ bands (Fig. S7(C)). Such coherence increase is also observed between θ and $\beta - \gamma$, while the δ versus θ pair shows a drop of the inter-band coherence. These wake-related coherent or incoherent events concern a wide range of modulation frequency from 2 to 2^{-8}Hz, that can be partly related to the subject motion.

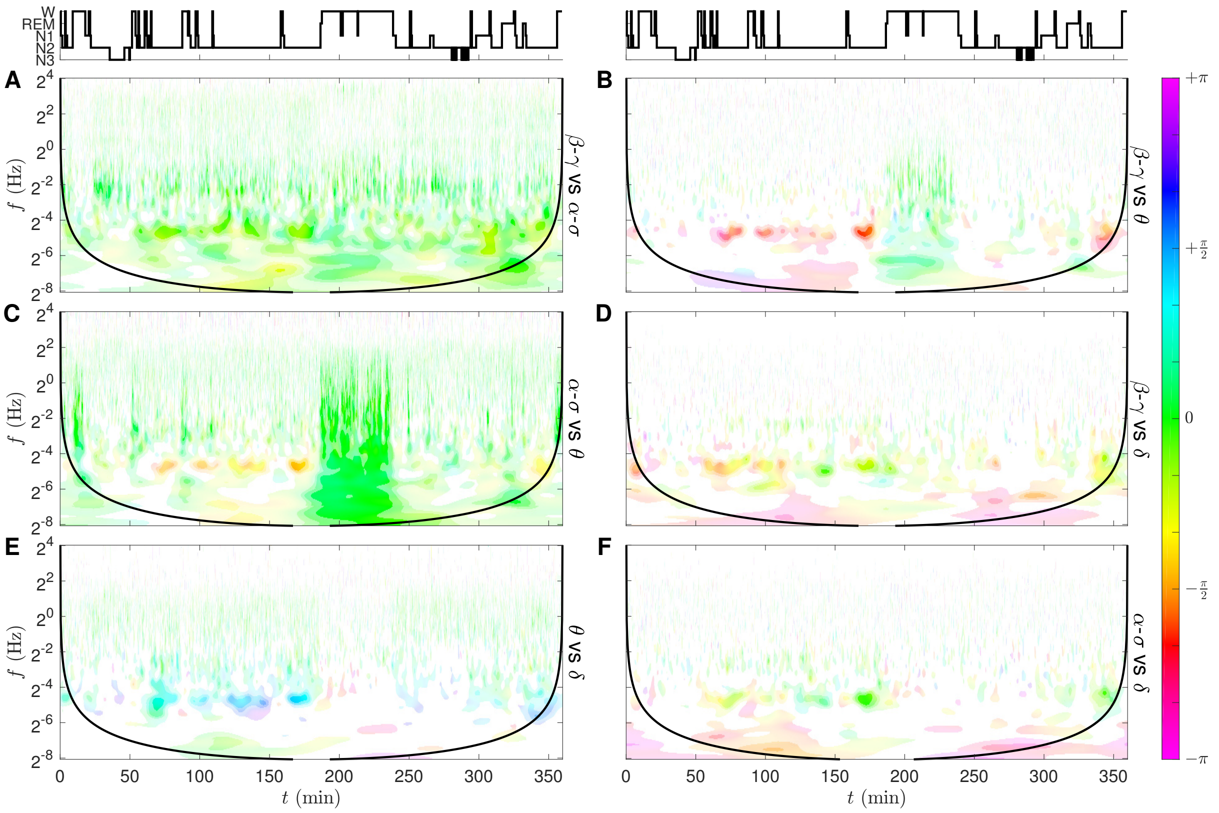

Figure S7. EEG inter-band time-frequency coherence, of the amplitude modulations whose CWTs are represented in Fig. S6. In the following, the coherence of signal x versus signal y corresponds to the quantity $\gamma_{xy}(f, t; Q, n)$. **(A)** $\beta - \gamma$ versus $\alpha - \sigma$ band, **(B)** $\beta - \gamma$ versus θ band, **(C)** $\alpha - \sigma$ versus θ band, **(D)** $\beta - \gamma$ versus δ band, **(E)** θ versus δ band, **(F)** $\alpha - \sigma$ versus δ band. The ranges of coherence moduli $|\gamma_{xy}|$ for the colour saturation coding are delimited by the lower thresholds $\gamma(10^{-1}) \approx 0.46,\ \gamma(10^{-3}) \approx 0.71,\ 0.8,\ 0.9$. The quality factor of the Grossmann wavelet is $Q = 5$ and the Gaussian time-smoothing parameter is $n = 10$. For each coherence image, a black line materializes a distance $n\delta t$ from the initial and final times, beyond which border effects are possible.

6 WAKE-SLEEP PATTERNS IN THE COHERENCE OF AN EEG PAIR

In this section, we illustrate our computation method of time-frequency coherence on two EEG signals, and we bring an additional demonstration of it richness for the analysis of complex physiological signals. We choose two EEGs recorded on both sides of the head of subject *205136* selected from the database *shhs2*. EEG_1 is measured between points C4-A1, and EEG_2 is measured between points C3-A2 (left-right symmetric to C4-A1). One would expect that these signals selected in contra-lateral positions would produce a very strong coherence, with little temporal evolution.

Their global coherence (complex extension of the correlation coefficient), estimated over the full overnight records (9 hours), is as low as $\rho^*_{21}(0) = 0.061 + i0.029$. In regard to the non-stationary and multi-scale characteristics of EEGs, this absence of global linear similitude is not much surprising. This does not mean that coherent time-frequency sub-domains could not occur, with different phases that interfere and globally cancel out. Therefore, we propose to localize the correlation analysis in different frequency bands and at different times by applying the time-frequency coherence formalism.

The succession of computations performed on these signals leading to γ_{21}, of EEG_2 versus EEG_1, is represented in Fig S8. We show in Fig S8(B,C) the signal and the shaded-colour coded CWT amplitude for EEG_1 only, those corresponding to EEG_2 have a very similar aspect. These CWTs need to be paired, multiplied and smoothed for the preliminary estimation of the power spectral densities. To keep the full frequency resolution offered by the wavelet analysis, we smooth in time only (see Gurley et al. (2003) for a similar use). We use the Gaussian time-smoothing kernel χ_n of width $n\delta t$ with $n = 50$ (δt is the wavelet duration). Notice how the patterns of the mean power density ($\sqrt{S_2(f,t)S_1(f,t)}f$, Fig. S8(D)) gives a clear illustration of the sleep stages (hypnogram (A) from the original annotations). The use of a large time-smoothing regime sets a low level of the spurious coherence ($\gamma_{\mathrm{sp}} \sim 0.14$), required for discriminating strong from weak correlations. It has however the side effect of a poor time resolution, especially below 0.5Hz (a quarter of an hour at $f = 0.2$Hz), where scattered coherent spots of varying phase are most likely due to isolated intense and coherent events such as motion artifacts. The quality factor $Q = 10$ is sufficient for an identification of the EEG bands (simultaneous modes of frequency ratio $\exp(\delta \log f) \approx 1.3$ can be distinguished).

Since the cross-spectrum $S_{21}(f,t)f$ is a complex valued map, we employ in Fig. S8(E) the amplitude-phase colour coding introduced in Fig. 2(D). Its phase (*i.e.* the one of the coherence) is an interesting information which we do not discard. It represents the phase difference between the signals: the zero phase shift is coded in green, the phase opposition ($\pm\pi$) is coded in magenta, and the phase quadrature is coded in orange ($-\frac{\pi}{2}$) or light blue ($+\frac{\pi}{2}$), as indicated in the colour bar. The strength of local correlations are finally obtained from the time-frequency coherence estimator $\gamma_{21}(f,t) = \gamma_{21}(f,t;Q,n)$ (Fig. S8(F), ratio of (E) and (D)). The regions of high in-phase coherence (green) during the REM stage (of low power), illustrates well the insensitivity of γ_{21} to the power density. The phase of the cross-spectrum remains, but its modulus is normalized so that a loss of coherence is only due to destructive phase interference. For a better readability, the saturation of the colours is discretized into 5 ranges of coherence modulus $|\gamma|$. The low coherence values that can not be distinguished from the spurious coherence (p-value $> 10^{-1}$) are in white (no saturation). The range represented with the faintest colour saturation is made of low but significant coherence values, with p-values $10^{-3} < p < 10^{-1}$: $|\gamma_{21}| \in [\gamma(10^{-1}),\ \gamma(10^{-3})] \approx [0.21,\ 0.36]$. The high coherence ranges are delimited by the coherence values $|\gamma| = \gamma(10^{-3}),\ 0.5,\ 0.7$ and 1, with increasingly saturated colours.

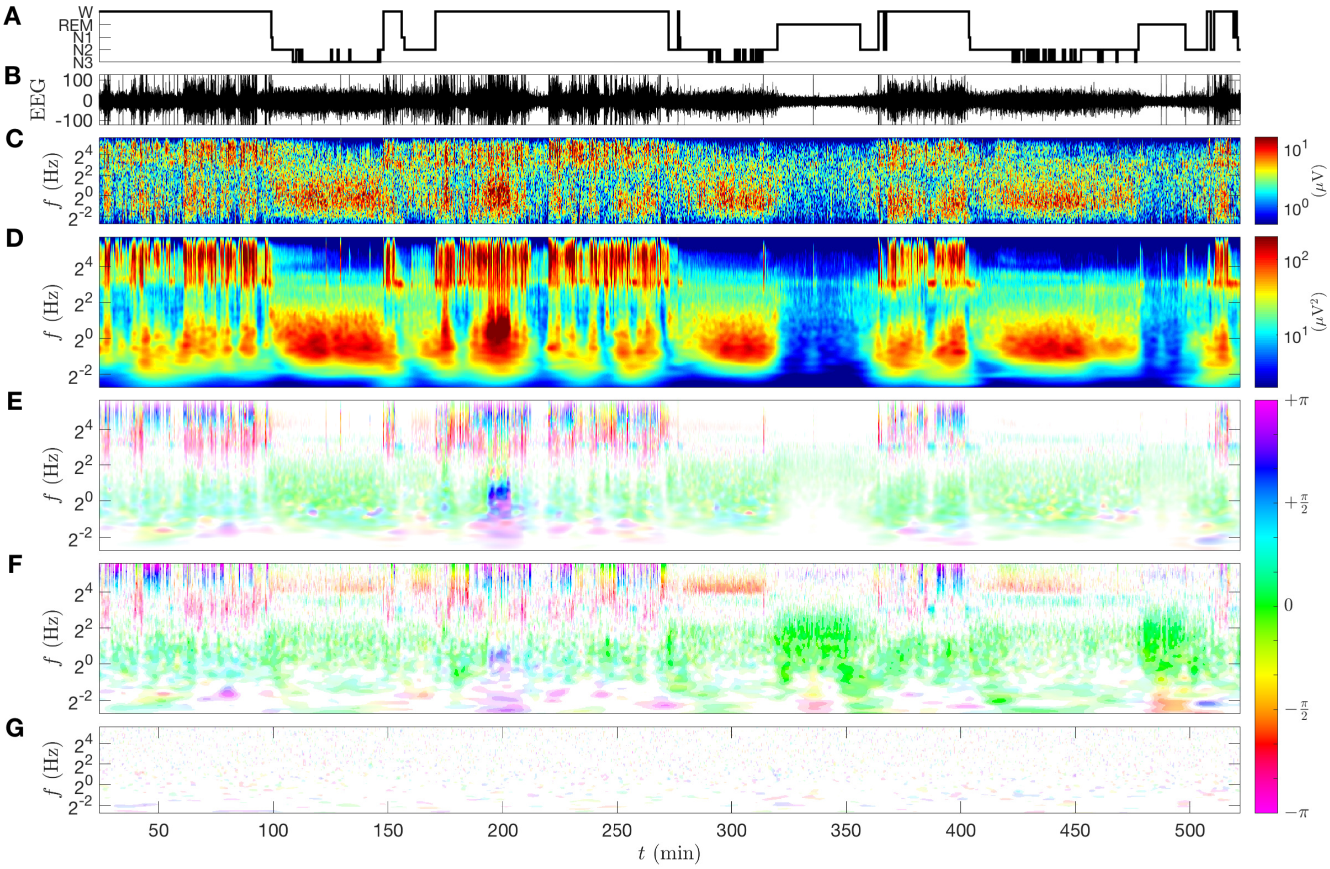

Figure S8. Time-frequency coherence analysis of two EEGs of subject *205136* from the database *shhs2*. EEG_1 corresponds to C4-A1 and EEG_2 to C3-A2. **(A)** Hypnogram. **(B)** EEG_1 (in μV). **(C)** Colour-coded amplitude of the CWT of EEG_1. **(D)** Geometric mean of the (time-varying) log-frequency power densities $\sqrt{S_2(f,t)S_1(f,t)}f$. **(E)** Cross power spectral density $S_{21}(f,t)f$ between EEG_2 and EEG_1. **(F)** Coherence $\gamma_{21}(f,t)$ (ratio of **E** and **D**). **(G)** Surrogate coherence, to illustrate the spurious coherence level in **(F)**. The ranges of coherence moduli $|\gamma_{21}|$ for the colour saturation coding are delimited by the lower thresholds $\gamma(10^{-1}) \approx 0.21,\ \gamma(10^{-3}) \approx 0.36,\ 0.5,\ 0.7$. The CWTs are computed with the Grossmann wavelet of quality factor $Q = 10$ and the power spectral densities are estimated from the Gaussian smoothing χ_n window, of temporal width $n = 50$ units of wavelet duration.

The expected spurious coherence level is illustrated by the surrogate time-frequency coherence (Fig. S8(G)), computed between independent signals (here the EEG and its phase-randomized surrogate signal) (Lancaster et al., 2018). Thus, the estimation of the significance for low coherence values can be controlled and visualized: the surrogate coherence only exhibits scattered spots of significance $10^{-3} < p < 10^{-1}$ (consistent with a density of false positives of about 10% in the time-frequency plane) with a random phase. The size of these spots is representative of the resolution of the coherence analysis in the time-frequency plane, and their area is constant in average (of the order of n time-frequency atoms). Its comparison to γ_{21} of Fig. S8(F) confirms that both EEG activities are strongly correlated, with various phase shifts, in many time-frequency regions.

Three main patterns can be distinguished, both from the time-frequency coherence (Fig. S8(F)) and from the power spectral density (Fig. S8(D,E)), which are clearly associated to the wake (W), NREM and REM states, as indicated in the hypnogram (A). In particular, the phase of the coherence is rich in information.

<table>
<tr><th></th><th>W</th><th>NREM</th><th>REM</th></tr>
<tr><td>γ</td><td>$++$P</td><td>$-$p</td><td>$+$p</td></tr>
<tr><td>β</td><td>$--$P</td><td>$--$p</td><td rowspan="2">0p</td></tr>
<tr><td>σ</td><td>bursts 0</td><td>$+$ $++$</td></tr>
<tr><td>α</td><td>$++$P $-$ 0</td><td>0p</td><td>liminal</td></tr>
<tr><td>θ</td><td>0 liminal</td><td>0</td><td rowspan="3">$++$p</td></tr>
<tr><td>δ^+</td><td>$+$P 0p</td><td>$+$</td></tr>
<tr><td>δ^-</td><td>bursts</td><td>0P $+$P</td></tr>
</table>

Table S1: Summary of the observation of the coherence $\gamma_{21}(f,t)$ between the central EEGs of the subject *205136* of the database *shhs2* (see Figs. S8 and S9). Different types of time-frequency regions are represented by the cells of the table. Rows indicate frequency bands (distinct or joint) while columns are time epochs corresponding to the three main states: wake (W), NREM (stages N2 and N3) and REM (N1 is considered to be a transient state between them). The bands δ^-, δ^+, θ, α, σ, β, γ are approximately delimited by the frequencies 0.25, 1, 4, 8, 12, 16, 20 and 60 Hz. In-phase coherence (positive correlation) is denoted by $(+)$, $(-)$ for phase opposition (anti-correlation), the sign is doubled for strong coherence moduli, (0) if incoherent. In addition, this code is completed by (**P**) (respectively p) for especially high (low) power spectral density. When the time-frequency pattern is heterogeneous, we qualify the fine structure as follows: several symbols in the same cell mean alternating or intermittent coherence, *bursts* stands for singular events, and *liminal* indicates an interstitial band influenced by neighbouring frequency bands.

The phase-frequency relation in all regions of significant coherence $\gamma_{21} = |\gamma_{21}|e^{i\phi_{21}}$ is well described by $\phi_{21} = \phi_\pm + 2\pi f\tau$, responsible for the vertical rainbows (phase gradients) at high frequencies in Fig. S8(E,F) (see also Fig S9(B) for a closer look). Remarkably, the first term of this linear relation can only take two angular values, $\phi_+ = 0$ and $\phi_- = \pm\pi$, and $\tau \approx 10$ms is a constant delay. Therefore, the left-right symmetry of the correlated EEG activity (that would write $\phi_{12} = \phi_{21}$) is only spoiled by a short delay: EEG_2 is 10ms early compared to EEG_1. Interestingly, this delay only corresponds to the third highest local maximum of the global correlation function. Its (complexified) value does not increase much, $\rho^*_{21}(\tau) = 0.085 + i0.019$, confirming the necessity of a time-frequency analysis to describe it.

In the light of this specific phase relation, the description of the coherence patterns boils down to: (i) the sign of the correlation, $(+)$ for in-phase regions ($\phi_+ = 0$) and $(-)$ for the ones in phase opposition ($\phi_- = \pm\pi$), and (ii) the strength of the coherence (insignificant to high). The time-frequency map of $\phi_\pm$ is obtained by compensating the delay: $\gamma_{21}(f,t)e^{-i2\pi f\tau}$ (illustrated in Fig S9(C)). The intense event at 200min and 1-2Hz (of phase $\sim \frac{\pi}{2}$, in blue) is an important deviation to this binary behaviour, which is certainly generated by motion artifacts. A synthetic description of the inter-EEG coherence in distinct time-frequency regions (EEG bands and sleep stages) for subject *205136* is constructed in Table S1. This confirms the strong relevance of this time-frequency coherence method to study sleep stages.

Fig. S9 provides a zoom of the power spectral density (A) and of the time-frequency coherence (B) of Fig. S8. The selected time-frequency domain contains the three main patterns of inter-EEG coherence (and power density) associated to distinct states: it starts with the end of NREM, then REM, wake and back to another NREM state.

The map $\gamma_{21}(f,t)e^{-i2\pi f\tau}$ in Fig. S9(C) provides a visual support to the detailed description of these patterns in Table 1. It consists in compensating the linear trend of the phase-frequency relation, caused by a global delay $\tau \approx 10$ms between the EEGs. It reveals that the intrinsic phase shifts are exclusively described by $\phi_+ = 0$ (in-phase, green) and $\phi_- = \pm\pi$ (phase opposition, magenta). For such a small delay, we notice

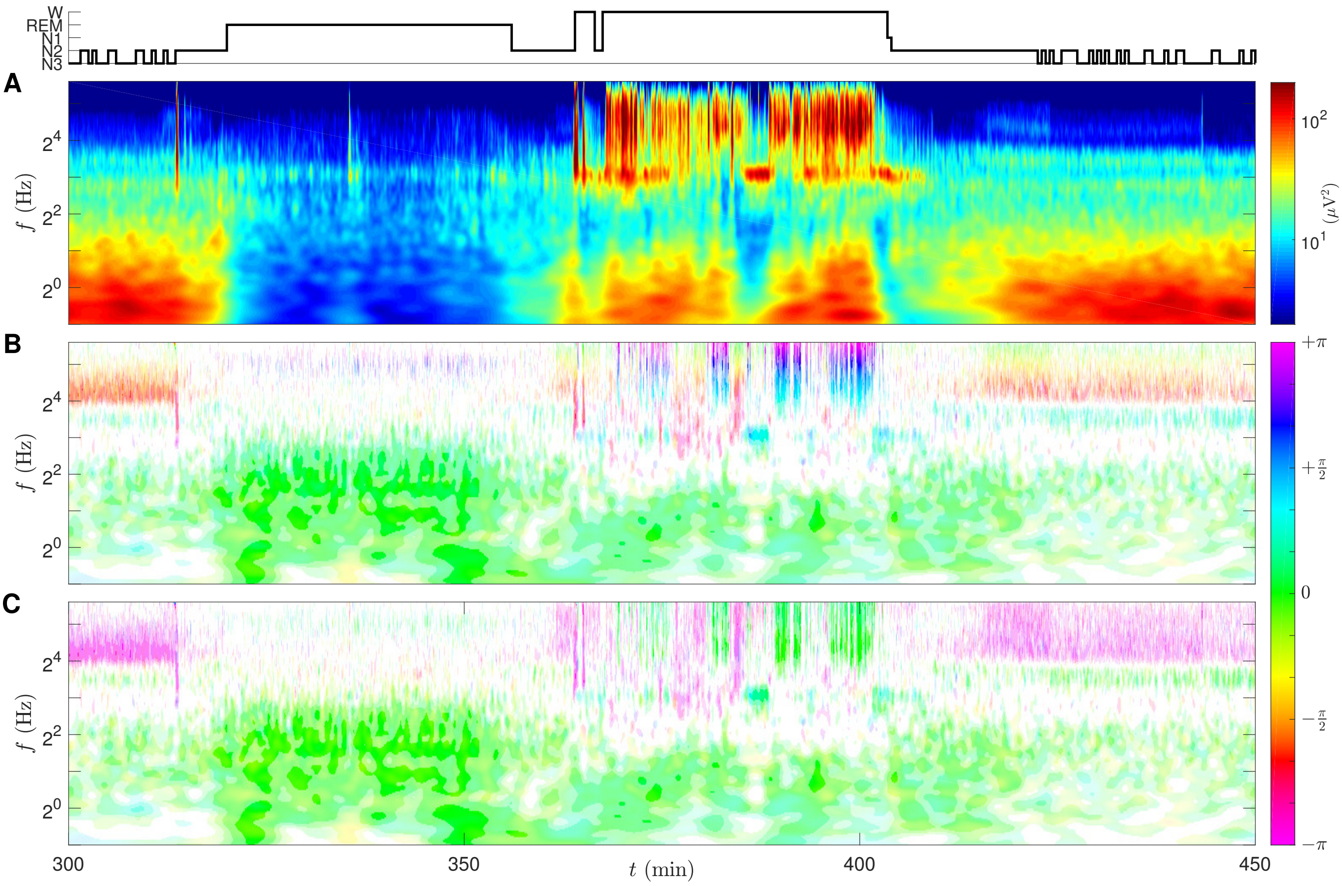

Figure S9. Details of the time-frequency coherence analysis of two EEGs of subject *205136* from the database *shhs2*. EEG_1 corresponds to C4-A1 and EEG_2 to C3-A2. **(A)** Geometric mean of the (time-varying) log-frequency power densities, $\sqrt{S_2(f,t)S_1(f,t)}f$. **(B)** Coherence $\gamma_{21}(f,t)$. **(C)** Coherence with the phase compensated by the global delay, $\gamma_{21}(f,t)e^{-i2\pi f\tau}$, where $\tau \approx 10$ms. The ranges of coherence moduli $|\gamma_{21}|$ for the colour saturation coding are delimited by the lower thresholds $\gamma(10^{-1}) \approx 0.21,\ \gamma(10^{-3}) \approx 0.36,\ 0.5,\ 0.7$. The CWTs are computed with the Grossmann wavelet of quality factor $Q = 10$ and the power spectral densities are estimated from the Gaussian smoothing χ_n window, of temporal width $n = 50$ units of wavelet duration.

that $\gamma_{21}(f,t)e^{-i2\pi f\tau}$ is a very precise approximation of the generalized coherence between $\mathrm{EEG}_2(t+\tau)$ and $\mathrm{EEG}_1(t)$: $\gamma_{21}(f,t+\tau,t)$.

REFERENCES

Brittain, J.-S., Halliday, D., Conway, B., and Jens Bo Nielsen (2007). Single-trial multiwavelet coherence in application to neurophysiological time series. *IEEE Transactions on Biomedical Engineering* 54, 854–862

Carter, G. (1987). Coherence and time delay estimation. *Proceedings of the IEEE* 75, 236–255

Cohen, E. and Walden, A. (2010a). A statistical analysis of morse wavelet coherence. *IEEE Transactions on Signal Processing* 58, 980–989

Cohen, E. A. K. and Walden, A. T. (2010b). A statistical study of temporally smoothed wavelet coherence. *IEEE Transactions on Signal Processing* 58, 2964–2973

Gardner, W. A. (1992). A unifying view of coherence in signal processing. *Signal Processing* 29, 113–140. doi:10.1016/0165-1684(92)90015-O

Gish, H. and Cochran, D. (1988). Generalized coherence. In *ICASSP, IEEE International Conference on Acoustics, Speech and Signal Processing - Proceedings* (IEEE), 2745–2748

Gurley, K., Kijewski, T., and Kareem, A. (2003). First and higher-order correlation detection using wavelet transforms. *Journal of Engineering Mechanics* 129, 188–201

Keissar, K., Davrath, L. R., and Akselrod, S. (2009). Coherence analysis between respiration and heart rate variability using continuous wavelet transform. *Philosophical Transactions of the Royal Society A: Mathematical, Physical and Engineering Sciences* 367, 1393–1406

Lancaster, G., Iatsenko, D., Pidde, A., Ticcinelli, V., and Stefanovska, A. (2018). Surrogate data for hypothesis testing of physical systems. *Physics Reports* 748, 1–60

Orini, M., Bailon, R., Mainardi, L. T., Laguna, P., and Flandrin, P. (2012). Characterization of dynamic interactions between cardiovascular signals by time-frequency coherence. *IEEE Transactions on Biomedical Engineering* 59, 663–673

Torrence, C. and Compo, G. P. (1998). A practical guide to wavelet analysis. *Bulletin of the American Meteorological Society* 79, 61–78

Walden, A. T. (2000). A unified view of multitaper multivariate spectral estimation. *Biometrika* 87, 767–788